

See discussions, stats, and author profiles for this publication at: <https://www.researchgate.net/publication/253234522>

# Two-Dimensional Computational Fluid Dynamics Simulation of Biomass Gasification in a Downdraft Fixed-Bed Gasifier with Highly Preheated Air and Steam

ARTICLE *in* ENERGY & FUELS · MAY 2013

Impact Factor: 2.79 · DOI: 10.1021/ef4003704

---

CITATIONS

8

---

READS

253

## 4 AUTHORS:



Yueshi Wu

KTH Royal Institute of Technology

4 PUBLICATIONS 25 CITATIONS

SEE PROFILE



Qinglin Zhang

KTH Royal Institute of Technology

10 PUBLICATIONS 112 CITATIONS

SEE PROFILE



Weihong Yang

KTH Royal Institute of Technology

119 PUBLICATIONS 1,205 CITATIONS

SEE PROFILE



Włodzimierz Błasiak

KTH Royal Institute of Technology

69 PUBLICATIONS 842 CITATIONS

SEE PROFILE

# Two-Dimensional Computational Fluid Dynamics Simulation of Biomass Gasification in a Downdraft Fixed-Bed Gasifier with Highly Preheated Air and Steam

Yueshi Wu,<sup>\*,†</sup> Qinglin Zhang,<sup>‡</sup> Weihong Yang,<sup>†</sup> and Wlodzimierz Blasiak<sup>†</sup>

<sup>†</sup>School of Industrial Engineering and Management, Department of Materials Science and Engineering, Division of Energy and Furnace Technology, KTH Royal Institute of Technology, SE-100 44 Stockholm, Sweden

<sup>‡</sup>Plasco Energy Group Incorporated, 1000 Innovation Drive, Suite 400, Ottawa, Ontario K2K 3E7, Canada

**ABSTRACT:** Biomass gasification is regarded as one of the most promising energy recovery technologies for the widespread use of biomass. Mathematical models have been developed to understand this process in downdraft fixed beds using zero- and one-dimensional models, but only a limited number of two-dimensional (2D) models for downdraft fixed-bed reactors can be found in the literature. In this study, a 2D computational fluid dynamics (CFD) model was developed to study the gasification process in a downdraft configuration, considering drying, pyrolysis, combustion, and gasification reactions. The gas and solid phases were resolved using an Euler–Euler multiphase approach, with exchange terms for the momentum, mass, and energy. The standard  $k-\epsilon$  turbulence model was used in the gas phase. The model results were compared to existing data from a demonstration-scale fixed-bed downdraft gasifier. The simulation results exhibit a reasonable agreement with the experimental data. Parameter studies were performed on the basis of the developed model, which indicated that an external heat source for the high-temperature agent gasification (HTAG) technology using superheated air combined with steam resulted in a limited combustion need in the gasifier and produced syngas with a high  $H_2$  fraction and low tar content, which is environmentally preferable.

## 1. INTRODUCTION

Biomass is currently the largest source of renewable energy, accounting for approximately 10–15% (or  $45 \pm 10$  EJ)<sup>1</sup> of the world's total energy supply. Markets for biomass heat appliances have enjoyed healthy growth in recent years, particularly in Europe. Gasification is regarded as one of the most promising energy recovery technologies for the widespread use of biomass. A recent advance in developing countries is the introduction of small-scale gasifier stoves for cooking.<sup>2</sup> The downdraft gasifier is a comparatively cheap reactor that can be used in small-scale projects for heat and power. Biomass gasifiers are complex facilities requiring time to be mounted and made operational, which makes it difficult to study their various working conditions.<sup>3</sup> For such an investigation, numerous models for downdraft fixed-bed gasifiers have been developed.

These models of biomass gasification in downdraft fixed-bed reactors can be categorized into two groups: (1) thermodynamic equilibrium models and (2) kinetic or non-equilibrium models. The thermodynamic equilibrium models, the so-called zero-dimensional (0D) models, are widely used among researchers<sup>4–8</sup> to predict the composition of the produced syngas and the equilibrium temperature by assuming that the chemical reactions reach equilibrium, but these models cannot provide highly accurate results and also cannot provide the concentration or temperature profiles inside the reactor as a lack of the transformation mechanisms. Because this approach is independent of the gasifier design, kinetic models, which take into account the reaction kinetics and the transfer phenomena among the phases, must be developed. This need spurred the development of one-dimensional (1D) biomass gasification models.<sup>9–12</sup> These models simulated the variations in the physical and chemical properties along the reactor height by considering the vertical

movements. To further this research, two-dimensional (2D) models are needed to comprehensively understand the gasification process and the effects of the reactor geometry. However, few works have performed 2D simulations of a downdraft fixed bed in the available literature.

In recent years, computational fluid dynamics (CFD) has been used as a powerful tool to build 2D or even three-dimensional (3D) models. Most of the reported CFD simulations for biomass gasification have been of entrained flow gasifiers.<sup>13,14</sup> Some researchers used the CFD approach to simulate the fast pyrolysis of biomass in fluidized-bed gasifiers.<sup>15,16</sup> Zhang et al.<sup>17</sup> performed the plasma gasification process of municipal solid waste using a 2D CFD model for an updraft fixed-bed gasifier. Gerun et al.<sup>18</sup> built a 2D axisymmetric CFD model for a two-state downdraft gasifier but only considered the oxidation zone.

In this study, a 2D CFD model was developed to study the biomass gasification process in a downdraft fixed-bed configuration, taking into account drying, pyrolysis, combustion and gasification reactions. The gas and solid phases were resolved using an Euler–Euler multiphase approach with exchange terms for the momentum, mass, and energy. All of the chemical reactions were defined within ANSYS FLUENT 14.5 using the user defined function (UDF). The model results were compared to existing data from a demonstration-scale fixed-bed downdraft gasifier using highly preheated air and steam, which was built at KTH Royal Institute of Technology. The effect of the operating parameters on the performance of the gasifier was then investigated.

Received: March 4, 2013

Revised: May 2, 2013

## 2. FACILITY AND FEEDSTOCK

**2.1. Experimental Setup.** A demonstration-scale high-temperature agent gasification (HTAG) test facility has been built at KTH Royal Institute of Technology. This system was described in a previous publication,<sup>19</sup> and a brief description of the gasifier is provided below.

The feedstock was filled from the top of a vertically cylindrical reactor using a continuous feeding system with four synchronized screws. The gasifying agent (the air/steam mixture) was preheated to 1303 K by a regenerative preheater that used an external fuel source to maintain a stable operation and was then introduced into the reactor from the side. The grate stopped biomass/char particles, resulting in a charcoal bed. The pyrolyzed gases were mixed with the gases produced by combustion and passed through the grate to generate the produced gases, which were sampled at the outlet of the gasifier. The temperatures were measured using thermocouple probes located at the centerline along the height of the reactor in different reaction zones. A schematic of the downdraft fixed-bed gasifier is presented in Figure 1.

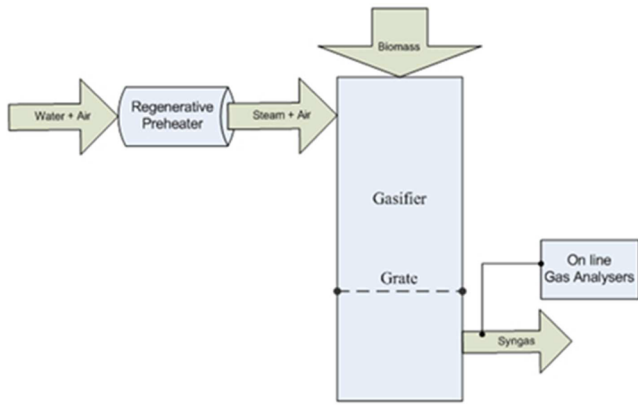


**Figure 1.** Schematic of the downdraft fixed-bed gasifier in the KTH Royal Institute of Technology laboratory.

**2.2. Fuel Parameters.** The feedstock used for the investigation was wood pellets, 0.008 m in diameter, with an average length/diameter ratio,  $l/d$ , of 4. The properties of the feedstock are shown in Table 1. The bulk density of the wood pellets is 630–650 kg/m<sup>3</sup>.

**Table 1.** Characterization of the Biomass Feedstock

proximate analysis		ultimate analysis (dry basis)	
moisture (%)	8	C (%)	50
volatiles (% dry basis)	84	H (%)	6.0–6.2
fixed carbon (% dry basis)	15.5	O (%)	43–44
ash (% dry basis)	0.5	N (%)	<0.2
		S (%)	0.01–0.02

## 3. NUMERICAL MODEL

This study applied the Euler–Euler multiphase flow framework. All of the species were divided into two phases: solid and gas. The conservation equations for the mass, momentum, and energy were solved for both phases. The exchanges of momentum (given by the drag between solid and gas phases), mass (given by the heterogeneous chemical reactions), and energy were allowed between phases and were described as source terms in the conservation equations. The standard  $k$ – $\epsilon$  turbulence model was used in the gas phase. A scheme of the multiphase model is shown in Figure 2.

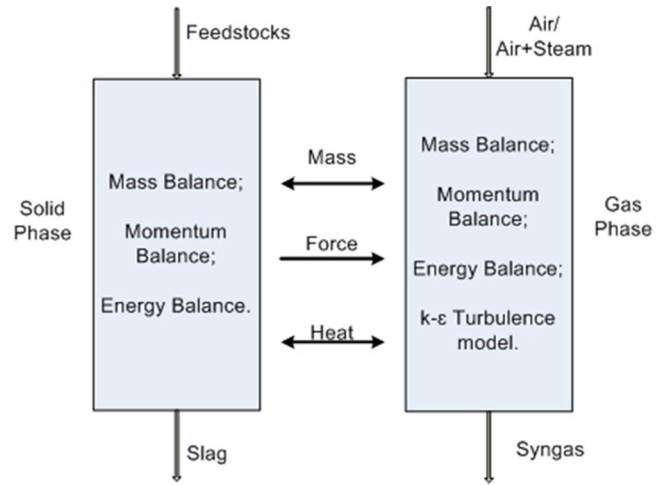


**Figure 2.** Schematic of the CFD model.

**3.1. Governing Equations.** The mass, momentum, and energy equations of the gas phase are described as follows:

$$\frac{\partial}{\partial t}(\alpha_g \rho_g Y_i) + \nabla(\alpha_g \rho_g Y_i \vec{v}_g) = \dot{m}_i + S_i \quad (1)$$

$$\begin{aligned} \frac{\partial}{\partial t}(\alpha_g \rho_g \vec{v}_g) + \nabla(\alpha_g \rho_g \vec{v}_g \vec{v}_g) \\ = -\alpha_g \nabla p + \nabla \vec{\tau}_g + \alpha_g \rho_g \vec{g} + K_{sg}(\vec{v}_s - \vec{v}_g) + \dot{m}_{sg} \vec{v}_{sg} \end{aligned} \quad (2)$$

$$\begin{aligned} \frac{\partial}{\partial t}(\alpha_g \rho_g h_g) + \nabla(\alpha_g \rho_g \vec{v}_g h_g) \\ = -\alpha_g \frac{\partial p}{\partial t} + \vec{\tau}_g : \nabla \vec{v}_g - \nabla \vec{q}_g + S_g + Q_{sg} + \dot{m}_{sg} h_{sg} \end{aligned} \quad (3)$$

The standard  $k$ – $\epsilon$  turbulence model<sup>20</sup> was used in the gas phase. The ideal gas law was used to calculate the gas density.

$$\rho_g = \frac{M}{R_g T_g} p \quad (4)$$

The governing equations for the solid phase are described as follows:

$$\frac{\partial}{\partial t}(\alpha_s \rho_s Y_j) + \nabla(\alpha_s \rho_s Y_j \vec{v}_s) = \dot{m}_j + S_j \quad (5)$$

$$\frac{\partial}{\partial t}(\alpha_s \rho_s \vec{v}_s) + \nabla(\alpha_s \rho_s \vec{v}_s \vec{v}_s) = -\alpha_s \nabla p - \nabla p_s + \nabla \vec{\tau}_s + \alpha_s \rho_s \vec{g} - \dot{m}_{sg} \vec{v}_{sg} \quad (6)$$

$$\frac{\partial}{\partial t}(\alpha_s \rho_s h_s) + \nabla(\alpha_s \rho_s \vec{v}_s h_s) = -\alpha_s \frac{\partial p}{\partial t} + \vec{\tau}_s : \nabla \vec{v}_s - \nabla \vec{q}_s + S_s + Q_{gs} - \dot{m}_{sg} h_{sg} \quad (7)$$

The flow of the solid phase was treated as a granular flow. The solid-phase stress consists of the solid pressure and shear stress. According to Cowin,<sup>21</sup> the flow of granular materials in a fixed-bed gasifier can be treated as a plastic flow. The Schaeffer model<sup>22</sup> can be used to describe the solid pressure,  $p_s$ , which can be written as<sup>23</sup>

$$p_s = \alpha_s p^* \quad (8)$$

$p^*$  is expressed by an empirical power law

$$p^* = A(\alpha_g - \alpha_g^*)^n \quad (9)$$

where  $\alpha_g^*$  is the minimum fluidized volume fraction of the gas phase. The empirical values of  $A = 10^{25}$  Pa and  $n = 10^{23}$  were used, which allow it to be used for the plastic flow regime.

Because the flow of the solid phase was a dense flow, the solid volume fraction of the solid phase was near the packing limit, which is 0.5. Therefore, we only considered the frictional viscosity for the shear stress portion. The shear stress can be calculated by<sup>24</sup>

$$\mu_s = \frac{p_s \sin \phi}{2\sqrt{I_{2D}}} \quad (10)$$

In a fixed-bed gasifier, the value of  $\nabla p_s$  is several orders of magnitude larger than the gas–solid stress.<sup>25</sup> Therefore, the influence of the gas–solid stress on the solid phase can be ignored. However, we considered this stress term in the gas phase, and it was calculated using the Ergun equation. The interphase momentum exchange coefficient,  $K_{sg}$ , is described as

$$K_{sg} = 150 \frac{\alpha_s(1 - \alpha_g)\mu_g}{\alpha_g d_s^2} + 1.756 \frac{\rho_g \alpha_s |\vec{v}_s - \vec{v}_g|}{d_s} \quad (11)$$

The interphase heat transfer is assumed to be a function of the temperature difference between the two phases

$$Q_{sg} = -Q_{gs} = k_{sg}(T_s - T_g) \quad (12)$$

where  $k_{sg}$  is the heat-transfer coefficient between the solid and gas phases. Convection is the main heat-transfer mechanism within the fixed-bed reactor, and  $k_{sg}$  is related with the Nusselt number and is expressed as

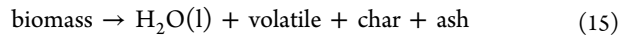
$$k_{sg} = \frac{6\kappa_g \alpha_g Nu_s}{d_s^2} \quad (13)$$

The Nusselt number was correlated by Gunn,<sup>26</sup> which is applicable for the void fraction of 0.35–1.0.

$$Nu_s = (7 - 10\alpha_g + 5\alpha_g^2)(1 + 0.7Re_s^{0.2}Pr_g^{0.33}) + (1.33 - 2.4\alpha_g + 1.2\alpha_g^2)Re_s^{0.7}Pr_g^{0.33} \quad (14)$$

**3.2. Reaction Models.** The source terms for the governing equations are determined by the rates of the chemical reactions in the gasifier. The biomass particle is dried after it is heated to the moisture vaporization temperature and is continuously heated to a temperature of approximately 673 K, at which the biomass particle is volatilized, resulting in volatile matter, char, and ash. After that, the char particle is burnt and gasified. Meanwhile, the gas phase reacts following a series of homogeneous chemical reactions.

The feedstock is considered to be a mixture of moisture, volatile matter, charcoal, and ash, as determined by the proximate analysis, following the equation:



The composition of the volatile matter is calculated by the ultimate analysis. Charcoal is simplified as the fixed carbon, and the composition of the ash is calculated from the elemental balance.

**3.2.1. Drying.** The moisture in the biomass is evaporated as the high-temperature gasifying agent transfers heat to the biomass.



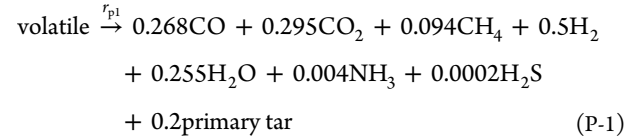
The drying rate is determined by the following expression, and it is assumed that the evaporation is assumed to be controlled by heat transfer:

$$r_d = A_s k_{sg}(T_s - T_{\text{evap}})/H_{\text{evap}} \quad (16)$$

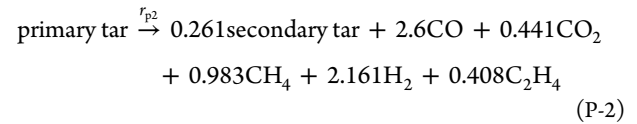
where  $A_s$  is the surface area of the solid particles ( $\text{m}^2$ ),  $H_{\text{evap}}$  is the heat of evaporation of water, which is 40.65 kg/mol, and  $T_{\text{evap}}$  is the saturation temperature, set to 375.15 K.

**3.2.2. Pyrolysis.** For simplification, the pyrolysis process is divided into primary pyrolysis and tar cracking using a two-step pyrolysis model.

primary pyrolysis



tar cracking



The pyrolysis reactions are considered to be under kinetic control. Tar is a complex mixture of hundreds of different organic species; however, the global compositions are used for both the primary and secondary tars in this study. The primary tar is expressed as  $\text{C}_{6.407}\text{H}_{11.454}\text{O}_{3.482}$ , which can be calculated from the elemental balance of the primary pyrolysis reaction. The secondary tar is assumed to be pure benzene, because experimental tests at KTH Royal Institute of Technology showed that 85% of the secondary tar was benzene.<sup>19</sup> The compositions of the product gas from the primary pyrolysis<sup>27</sup> and tar cracking<sup>28</sup> reactions are estimated on the basis of the literature data obtained for wood.

The reaction rates are calculated by<sup>29,30</sup>

$$r_{p1} = 4.38 \times 10^9 (1 - \alpha_g) \exp\left(\frac{-1.527 \times 10^5}{RT_s}\right) C_{\text{volatile}} \quad (17)$$

$$r_{p2} = 4.28 \times 10^6 \alpha_g \exp\left(\frac{-1.08 \times 10^5}{RT_g}\right) C_{\text{primary tar}} \quad (18)$$

**3.2.3. Char Reactions.** The heterogeneous char reactions are considered using the unreacted shrinking core model. It assumes that the char particles are spherical grains and that the reaction between the char particles and the gas is initiated on the external surface. The reaction will move step-by-step to the interior, which forms an interior unreacted core and an exterior ash layer. The chemical reaction rates ( $r_m$ ) of the char reactions are determined by the film mass-transfer coefficient diffusion ( $s_m$ ) and the kinetic reaction rates ( $r_{km}$ ). The chemical reaction rates are written as

$$r_m = \left(\frac{1}{v_i M_i}\right) \frac{A_v \rho_i}{\frac{1}{s_m} + \frac{1}{r_{km}}} \quad m = 8-11 \quad (19)$$

where  $i$  represents the gaseous reactants of reaction  $m$ .

The char combustion and gasification reactions considered in this model and the kinetic reaction rates are summarized in Table 2. The film mass-transfer coefficient is described as<sup>31</sup>

$$s_m = \frac{2.06G}{\alpha_g \rho_g} Re^{-0.575} Sc^{-2/3} \quad (20)$$

where  $G$  is the gas mass flux in  $\text{kg m}^{-2} \text{s}^{-1}$ .

Table 2. Kinetic Reaction Rates of the Char Reactions

	reactions	kinetic reaction rate (m/s)	reference
R-C-1	$2C + O_2 \xrightarrow{r_{k8}} 2CO$	$r_{k8} = 2.30T_g \exp(-11100/T_g)$	33
R-C-2	$C + O_2 \xrightarrow{r_{k9}} CO_2$	$\frac{r_{k8}}{r_{k9}} = 2512 \exp(-6420/T_g)$	34
R-C-3	$C + H_2O \xrightarrow{r_{k10}} CO + H_2$	$r_{k7} = 5.714T_g \exp(-15600/T_g)$	35
R-C-4	$C + CO_2 \xrightarrow{r_{k11}} 2CO$	$r_{k8} = 5.89 \times 10^2 T_g \exp(-26800/T_g)$	33

Table 3. Kinetic Reaction Rates of the Homogeneous Reactions

	reactions	kinetic reaction rate (kmol m <sup>-3</sup> s <sup>-1</sup> )	reference
R-G-1	primary tar + O <sub>2</sub> $\xrightarrow{r_{k1}}$ H <sub>2</sub> O + CO	$r_{k1} = 59.8T_g^{0.3} \alpha_g \exp(-12200/T_g) C_{\text{primary tar}}^{0.5} C_{O_2}$	36
R-G-2	secondary tar + O <sub>2</sub> $\xrightarrow{r_{k2}}$ H <sub>2</sub> O + CO	$r_{k2} = 59.8T_g^{0.3} \alpha_g \exp(-12200/T_g) C_{\text{secondary tar}}^{0.5} C_{O_2}$	36
R-G-3	H <sub>2</sub> + 1/2O <sub>2</sub> $\xrightarrow{r_{k3}}$ H <sub>2</sub> O	$r_{k3} = 3.53 \times 10^{8.4} \alpha_g \exp(-3670/T_g) C_{H_2}^{1.1} C_{O_2}^{1.1}$	37
R-G-4	CO + 1/2O <sub>2</sub> $\xrightarrow{r_{k4}}$ CO <sub>2</sub>	$r_{k4} = 1.3 \times 10^{11} \alpha_g \exp(-15105/T_g) C_{CO} C_{H_2O}^{0.5} C_{O_2}^{0.5}$	38
R-G-5	CO + H <sub>2</sub> O $\xrightleftharpoons{r_{k5}}$ H <sub>2</sub> + CO <sub>2</sub>	$r_{k5} = 2.78 \alpha_g \exp(-1511/T_g) \left( C_{CO} C_{H_2O} - \frac{\exp(-7914/T_g) C_{CO_2} C_{H_2}}{0.0265} \right)$	35 and 39
R-G-6	CH <sub>4</sub> + 1.5O <sub>2</sub> $\xrightarrow{r_{k6}}$ CO + 2H <sub>2</sub> O	$r_{k6} = 1.0 \times 10^{11.7} \alpha_g \exp(-24357/T_g) C_{CH_4}^{0.7} C_{O_2}^{0.8}$	40
R-G-7	CH <sub>4</sub> + H <sub>2</sub> O $\xrightarrow{r_{k7}}$ CO + 4H <sub>2</sub>	$r_{k7} = 3.0 \times 10^8 \alpha_g T_g \exp(-15083/T_g) C_{CH_4} C_{H_2O}$	41

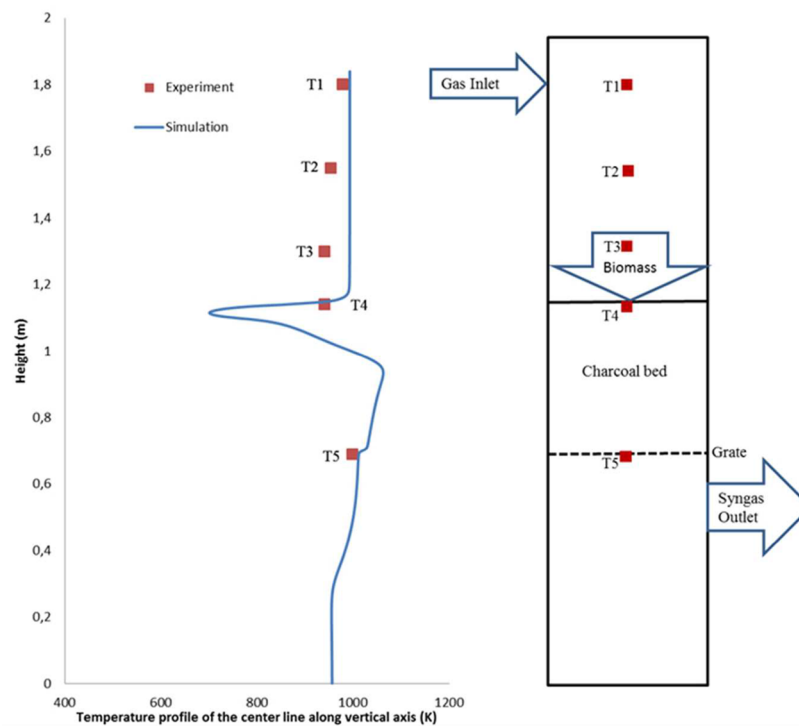


Figure 3. Experimental and simulated temperature distributions for the centerline along the vertical axis inside the gasifier.

**3.2.4. Homogeneous Reactions.** The gas-phase species included in this model are O<sub>2</sub>, N<sub>2</sub>, H<sub>2</sub>, CO, CO<sub>2</sub>, H<sub>2</sub>O(g), CH<sub>4</sub>, C<sub>2</sub>H<sub>4</sub>, H<sub>2</sub>S, NH<sub>3</sub>, primary tar, and secondary tar.

An overview of chemical reactions in the gas phase and their kinetic reaction rates is presented in Table 3.

The chemical reaction rates are determined by the minimum value of the kinetic reaction rates ( $r_{km}$ ) and the turbulent mixing rates ( $r_{tm}$ ).

$$r_m = \min(r_{km}, r_{tm}) \quad m = 1-7 \quad (20)$$

The turbulent mixing rates are estimated using the eddy dissipation (ED) model

$$r_{tm} = 4.0 \rho \frac{\varepsilon}{k} \min \left( \frac{Y_i}{\nu_i M_i}, \frac{Y_j}{\nu_j M_j} \right) \quad (21)$$

where  $i$  and  $j$  denote the reactants of reaction  $m$ .



## 4. RESULTS AND DISCUSSION

**4.1. Comparison to Experimental Data.** The experimental data reported in our previous publication<sup>32</sup> are compared to the simulation results. The operating conditions of the experiment are taken as the boundary conditions for the simulation. The model uses a gasifying agent inlet on the topside and a syngas outlet at the opposite side, under the grate. The biomass was fed from the top of the gasifier in the experiment. Because the main study is focused on the charcoal bed, in the model, the biomass input is relocated to be 0.45 m above the grate, which is the same position as the height of the initial charcoal bed in the experiment.

For the comparison case, the mass flow rate of the feedstock is 60 kg/h. The hot gasifying agent is feed at a mass flow rate of 106.3 kg/h and a temperature of 1303 K, in which the steam/air mass ratio (S/A) is 0.89. In the real process, significant heat was lost before the gasifying agent entered the reactor. Therefore, the temperature T1, which was measured after the inlet of the gasifying agent and had a value of 973 K, is taken as the preheating temperature in the model.

Figure 3 compares the temperature distribution for the center line along the vertical axis predicted by the model to the experimental results.

The predicted temperature was in reasonable agreement with the testing points, especially at three important points: after the feed gas entered the reactor (T1), the top of the charcoal bed (T4), and under the grate (T5). As expected, a significant temperature drop can be observed underneath the top of the charcoal bed because of the heat exchange between the cold feedstock and hot gasifying agent and also because of the endothermic drying and pyrolysis reactions. The temperature then increased, which showed the formation of the combustion zone. The gasification reactions are mainly endothermic reactions, which might be the main reason for the temperature drop after the combustion.

Figure 4 compares the produced gas compositions predicted by the model to the experimental values. The species compared

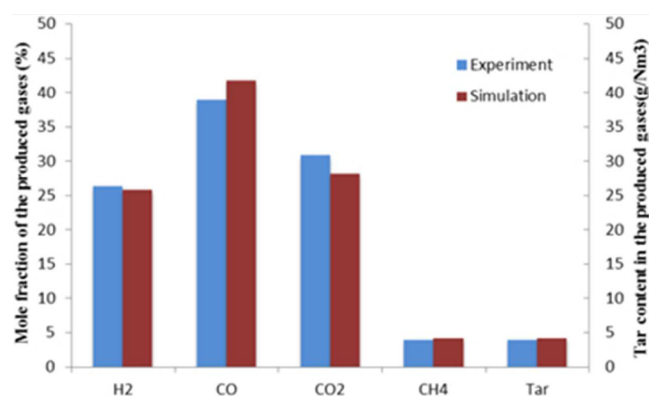


**Figure 4.** Comparison of the simulated produced gas compositions to the experimental values.

are the main combustible products, CO<sub>2</sub>, and tar generated during the gasification process. It can be seen that both the predicted and experimental data showed similar compositions. For both, the mole fractions of H<sub>2</sub> and CH<sub>4</sub> are approximately 26 and 4.1%, respectively, with a tar content of 4 g/Nm<sup>3</sup>. The predicted produced gas has a higher CO content than found in the experimental data but is the opposite for CO<sub>2</sub>. This result might be because the air that entered the reactor along with the

feed biomass reacted with CO to generate CO<sub>2</sub>. However, the deviation is less than 8%, with the CO<sub>2</sub> fraction showing the largest deviation. Therefore, this model is acceptable to analyze the performance of the HTAG (air/steam mixture) process in the downdraft fixed-bed gasifier.

**4.2. Parameter Study.** The performance of the gasifier is directly influenced by the chosen operating conditions. In this study, the examined parameters were the S/A ratio and preheating temperature of the gasifying agent. Each operating parameter was varied while keeping the other parameter constant. The mass flow rates of the feedstock and air were 60 and 56.3 kg/h, respectively, for all of the cases. The basic conditions were a S/A ratio of 0.89 and a preheating temperature of 1303 K for the gasifying agent.

**4.2.1. Analysis of the Basic Case.** The basic case was studied from two points: the gas temperature distributions in the horizontal direction and the average gas composition profile in the vertical direction.

Figure 5 shows the gas temperature distributions for different horizontal sections in the charcoal bed. The figure shows that the

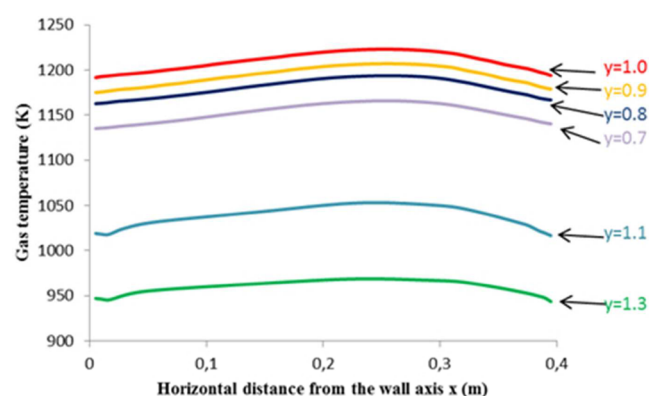


**Figure 5.** Gas temperature distribution for different horizontal sections in the charcoal bed.

temperature distribution in a horizontal section is not uniform, which is due to the uneven fluid field because the geometries of the gas inlet and outlet are asymmetrical. The peak temperatures in the different sections appear at  $0.23 < x < 0.29$  m. In this model, the walls (except for the top wall) are to be considered adiabatic. The peak temperature most likely could be explained by the char combustion that occurs in a certain layer near the gas–bed interface. The average temperature of  $y = 1.13$  m is much lower than the other positions. At this point, the biomass meets with the hot gas and the drying reaction occurs. The temperature is the highest at  $y = 1.0$  m; here, the char combustion is enhanced. The heat from the combustion was combined with the sensible heat and carried by the hot agent; this energy was consumed by the pyrolysis at  $y = 1.1$  m and gasification at  $y = 0.7–0.9$  m.

Figure 6 shows the profiles of the average gas composition along the vertical direction of the gasifier. The charcoal bed was located from 0.69 to 1.14 m. The biomass met with the hot agent at 1.14 m. The drying reaction was begun, and the moisture content in the biomass particle was released, which can be observed from the first peak of the steam content. The drying reaction could also explain the temperature drop in this area in Figure 5. The other peak for steam denoted where the primary pyrolysis, which has steam as a product, took place; this can also be confirmed by the appearance of H<sub>2</sub> and CH<sub>4</sub>.

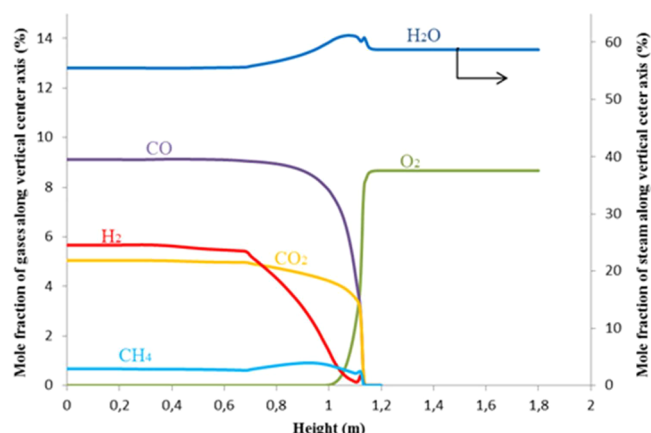


Figure 6. Profiles of the average gas composition along the vertical axis.

The gasification and combustion zones could be differentiated on the basis of the presence or absence of free oxygen. Oxygen was totally assumed at the  $y = 1$  m position, which indicated the consummation of the combustion reactions. This was verified by the occurrence of the highest temperature at the same place in Figure 5.

In reality, gasification and combustion typically occur at the same time. Figure 6 shows that the rate of generation of CO is faster than that of CO<sub>2</sub> after the point of  $y = 1.13$ . Some of the reactions that can be used to explain this result include R-C-3, R-C-4, and R-G-7.

When no free oxygen exists, the only reaction that consumes CH<sub>4</sub> is R-G-7. The mole fraction of CH<sub>4</sub> has a peak at approximately  $y = 0.95$ , when no free oxygen existed. At this point, two reactions related to CH<sub>4</sub> occur. The R-G-7 reaction consumes CH<sub>4</sub>; therefore, we can say that the CH<sub>4</sub> peak is caused by the tar-cracking reaction. After all of the reactions reached equilibrium, the composition of the gases will not change.

**4.2.2. Effect of the Preheating Temperature.** Figure 7 shows the temperature of the gas phase and the mass concentration profiles of the tars during gasification with different preheating temperatures for the feed gas, ranging from 1103 to 1503 K. The peak temperature inside the charcoal bed increased as the preheating temperature increased. This is because the sensible heat carried by the hot feed gas induced an increase in the temperature of the bed. The positive impacts of the higher bed temperature were higher chemical reaction rates and enhanced heat transfer. At the same time, the drying zone was significantly narrowed. A consequence of the higher bed temperature was a relative decrease in the biomass residence time, which made the HTAG technology more insensitive to variabilities in the heating value and moisture content of the biomass and the particle size.

Figure 7 demonstrates that the primary tar began to be consumed (the secondary tar began to appear) at a higher position when the preheating temperature was increased. This finding is observed because the required activation energy for the tar-cracking reaction was reached more quickly using a higher preheating temperature. Therefore, for the same residence time of biomass, more time remained for tar cracking. However, a high temperature is also an important factor in increasing the tar combustion reaction rate. Consequently, the tar content decreased with higher feed gas preheating temperatures.

Figure 8 shows the influence of the feed gas preheating temperature on the composition of the dry produced gases. It could be observed that, for the same S/A ratio (0.89), the mole fraction

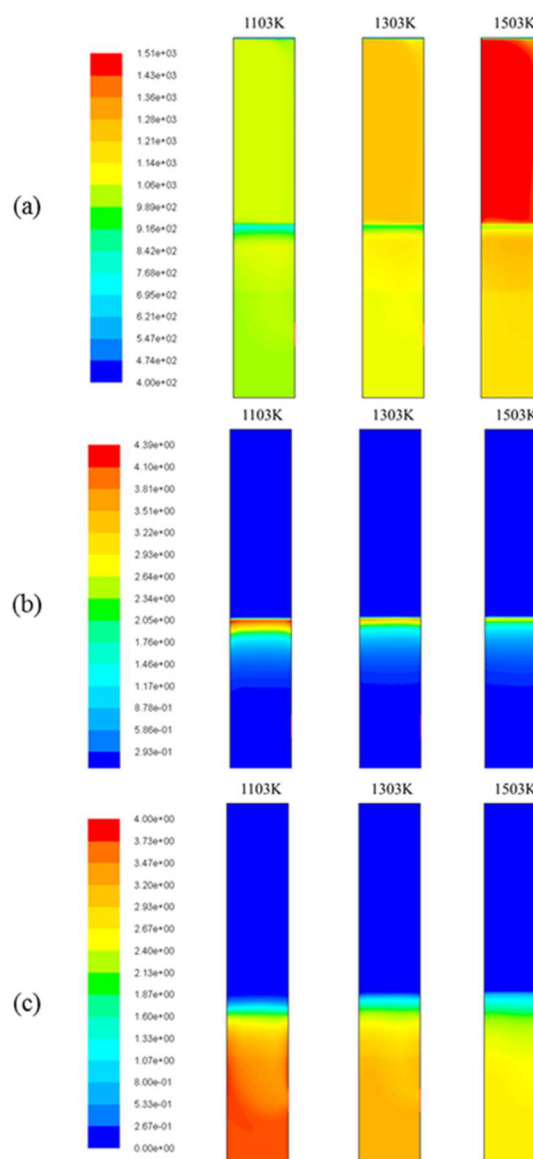


Figure 7. Gas-phase parameters for different preheating temperatures: (a) temperature (K), (b) mass concentration of the primary tar ( $\text{g/Nm}^3$ ), and (c) mass concentration of the secondary tar ( $\text{g/Nm}^3$ ).

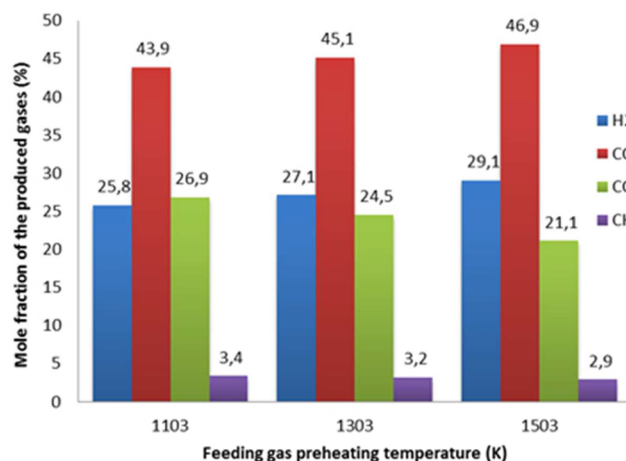


Figure 8. Influence of the feed gas preheating temperature on the composition of the produced gases.

of  $H_2$  continuously increased from 25.8 to 29.1% within the preheating temperature range of 1103–1503 K. The same trend can be observed for the mole fraction of CO, which increased from 43.9 to 46.9%. The observed increases are results of the pyrolysis and tar-cracking reactions, which are favored by the increase in the temperature because a high temperature would promote higher reaction rates and result in a greater production of the combustible components of the produced gases. As expected, the mole fraction of  $CO_2$  significantly decreased as the preheating temperature increased. The high temperature increased the activity of the char gasification reactions (R-C-3 and R-C-4).  $CO_2$  was consumed by the gasification reactions, with corresponding increases in the fractions of CO and  $H_2$ . The mole fraction of  $CH_4$  decreased from 3.37 to 2.9%, which was affected by the increased rate of reaction R-G-7 at a higher temperature. However, the variation in  $CH_4$  was relatively small compared to those of  $H_2$ , CO, and  $CO_2$ .

The most pronounced effect of preheating could be observed in the increase in  $H_2$ , which is calculated by the increase in the  $H_2/CO$  mole ratio from 0.58 to 0.62. At the same time, the  $H_2/CO_2$  mole ratio increased from 0.96 to 1.38. The  $CO/CO_2$  mole ratio increased from 1.63 at 1103 K to 2.22 at 1503 K. The results clearly indicate that the more favorable conditions for reaction R-C-4 occur at higher preheating temperatures.

**4.2.3. Effect of the S/A Ratio.** The heat needed for the decomposition of the biomass can be supplied by the partial oxidation of the feedstock by supplying air or other forms of external heat. In this work, the partial oxidation of the biomass and the sensible heat of the preheated steam and air mixture provide the heat required for the decomposition of biomass. The influence of the S/A ratio on the HTAG process was studied by varying the steam feed rate while maintaining a constant air feed rate. Figure 9 presents the distributions of the gas-phase temperature and concentration of the tars as the S/A ratio was varied from 0.71 to 1.07. Although at higher S/A ratios, more sensible heat was entering the reactor via the steam, the gas temperature inside the bed did not change significantly. Because gasification with steam is a highly endothermic process, the sensible heat carried by the gasifying agent might be consumed by the steam gasification reactions under the operating conditions in this work.

The results indicate that the increase in the S/A ratio is beneficial in reducing the tar content. In this study, the S/A ratio was changed by varying the steam feed rate while maintaining a constant air feed rate. A portion of the required heat came from the sensible heat carried by the additional steam when the S/A ratio was increased. As a result, the saved oxygen could react with the tar, which might be the reason for the tar reduction.

Figure 10 shows the compositions of the gases produced using a mixture of air and steam at different S/A ratios as the gasification agent. When the S/A ratio increased from 0.71 to 1.07, the formation of  $H_2$  increased from 25.5 to 27.9%. This could be explained because reactions R-C-3 and R-G-5 involve steam and might be favored by increasing the steam in the feed gas. In this same S/A ratio range, the mole fraction of CO exhibited a steadily decreasing trend from 47.8 to 44.0%. Meanwhile, the mole fraction of  $CO_2$  showed the opposite trend. These results could be explained by reaction R-G-5. This homogeneous so-called water–gas shift reaction is a purely gaseous reaction, which takes place in the presence of steam. The partial pressure of water vapor increased by adding steam, which forced the reaction to the products. Additionally, the combination of reaction R-G-7 with reaction R-C-3 could also explain the formation of CO. The mole

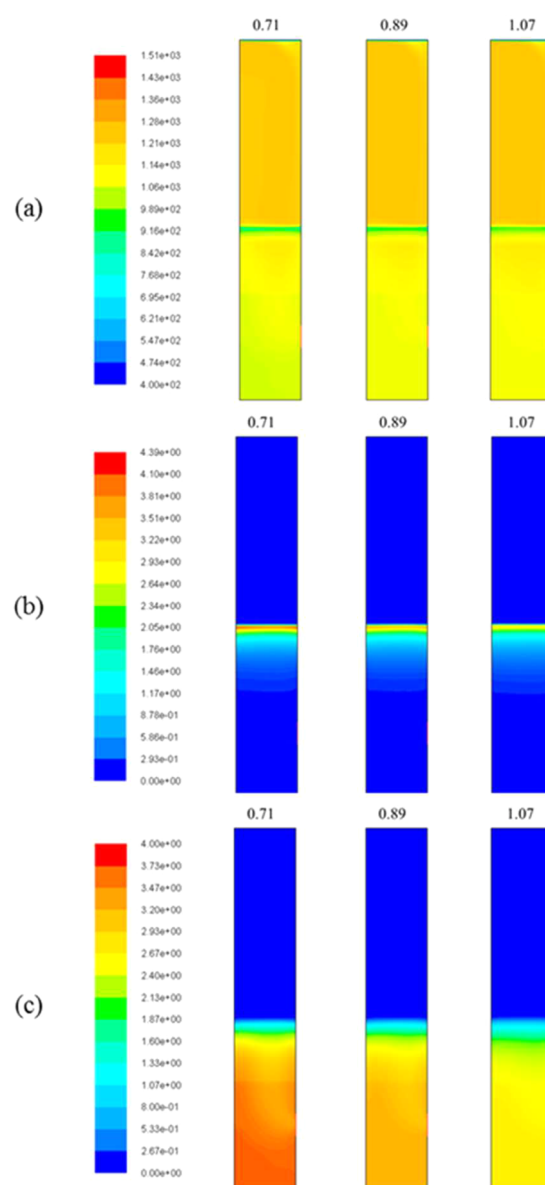


**Figure 9.** Gas-phase parameters for different S/A ratios: (a) temperature (K), (b) mass concentration of the primary tar ( $g/Nm^3$ ), and (c) mass concentration of the secondary tar ( $g/Nm^3$ ).

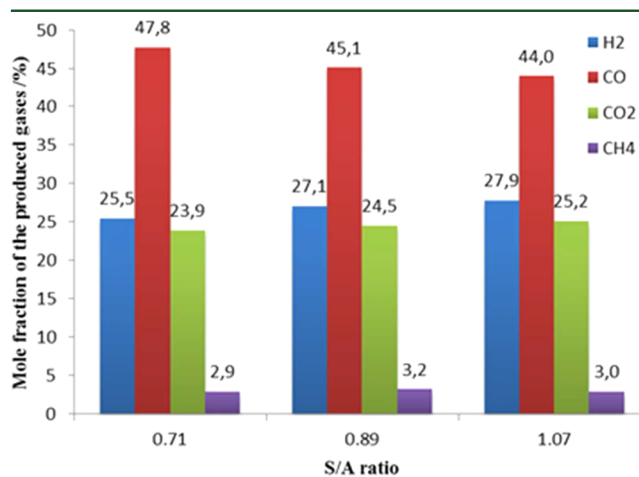


**Figure 10.** Influence of the S/A ratio on the composition of the produced gases.



fraction of CH<sub>4</sub> exhibited an irregular trend because the S/A ratio was varied and reached a maximum value of 3.2% when the S/A ratio was 0.89. Reaction R-G-7 is reversible; therefore, when it reaches a balance, adding steam will not further affect the reaction.

## 5. CONCLUSION

A 2D CFD model of a downdraft fixed-bed gasifier was developed. The simulation results were compared to experimental data and showed that the model can reasonably predict the temperature profile and the composition of the gases during the HTAG process.

The basic case was analyzed, and parameter studies were carried out on the temperature and gas composition profiles to assess the effects of the preheating temperature and the S/A ratio.

In the gasifier, the temperature distribution is not uniform in a given horizontal section. The peak temperatures in different sections appear at  $0.23 < x < 0.29$  m, which could be explained by the occurrence of char combustion in a certain layer near the gas–bed interface.

The increase in the feed gas preheating temperature will lead to a higher bed temperature and a relatively decreased required biomass residence time, which makes the HTAG technology more insensitive to variability. Additionally, the positive effects of higher preheating temperatures are an increase in the combustible gases (H<sub>2</sub> and CO) and a decrease in the tar produced.

The increase of the S/A ratio is also beneficial in reducing the tar content. Hence, at higher S/A ratios, the mole fractions of H<sub>2</sub> and CO<sub>2</sub> were high and that of CO was low. The CH<sub>4</sub> content showed a peak value that was determined by the balance of the pyrolysis reactions (which produce CH<sub>4</sub>) and the methane–water shift reaction (which consumes CH<sub>4</sub>).

Conventional gasification technologies rely on the combustion inside the process itself to sustain the reaction. However, the HTAG technology relies on an external heat source and uses superheated air combined with steam, which results in a limited need for combustion within the gasifier and produces syngas with a high H<sub>2</sub> fraction and low tar content, which is environmentally preferable.

## AUTHOR INFORMATION

### Corresponding Author

\*Telephone: +46-8-790-90-22. E-mail: yueshiw@kth.se.

### Notes

The authors declare no competing financial interest.

## ACKNOWLEDGMENTS

The financial support of this work by KIC InnoEnergy is gratefully acknowledged.

## NOMENCLATURE

$A_i$  = pre-exponential factor of reaction  $i$

$A_v$  = specific surface area (m<sup>-1</sup>)

$A_s$  = surface area of solid particles (m<sup>2</sup>)

$C$  = mass concentration (kg/m<sup>3</sup>)

$d_s$  = particle diameter (m)

$D$  = diffusion coefficient of the vapor in the bulk (m<sup>2</sup>/s)

$E_i$  = activation energy of reaction  $i$

$\vec{g}$  = gravitational acceleration (m/s)

$g$  = gas phase

$h$  = specific enthalpy (J/kg)

$H_{\text{evap}}$  = heat of evaporation of water (kg/mol)

$k$  = heat-transfer coefficient (W m<sup>-2</sup> K<sup>-1</sup>)

$\dot{m}$  = mass-transfer rate (kg m<sup>-3</sup> s<sup>-1</sup>)

$M$  = molar weight (kg/kmol)

$\dot{M}$  = mass flow rate (kg/s)

$p$  = pressure (Pa)

$q$  = heat flux (W/m<sup>2</sup>)

$Q$  = interphase heat transfer (W/m<sup>3</sup>)

$r$  = reaction rate (kmol m<sup>-3</sup> s<sup>-1</sup>)

$r_{ki}$  = kinetic rate of chemical reaction  $i$  (m/s)

$r_{ti}$  = turbulent mixing rate of reactants in reaction  $i$  (kmol m<sup>-3</sup> s<sup>-1</sup>)

$R$  = universal gas constant (J mol<sup>-1</sup> K<sup>-1</sup>)

$s$  = solid phase

$S$  = source term

$t$  = time (s)

$T$  = temperature (K)

$v_1$  = volatile from wood pellet species

$\vec{v}$  = velocity (m/s)

$v_i$  = stoichiometric coefficient of reactant  $i$

$Y_i$  = mass fraction of species  $i$

$\alpha$  = volume fraction

$\rho$  = density (kg/m<sup>3</sup>)

$\vec{\tau}$  = stress tensor (Pa)

$\mu$  = dynamic viscosity (Pa s)

$\phi$  = angle of internal friction

$\kappa$  = thermal conductivity (W m<sup>-1</sup> K<sup>-1</sup>)

$\epsilon$  = turbulent dissipation rate (m<sup>2</sup>/s<sup>3</sup>)

## REFERENCES

- (1) Saidur, R.; et al. A review on biomass as a fuel for boilers. *Renewable Sustainable Energy Rev.* **2011**, 15 (5), 2262–2289.
- (2) Sawin, J. L. Renewables 2012. In *Global Status Report*; Mastny, L., Ed.; Renewable Energy Policy Network for the 21st Century (REN21): Paris, France, 2012; p 33.
- (3) Vaezi, M.; et al. Modeling biomass gasification: A new approach to utilize renewable sources of energy. *ASME Conf., Proc.* **2008**, No. 48692, 927–935.
- (4) Jarungthammachote, S.; Dutta, A. Thermodynamic equilibrium model and second law analysis of a downdraft waste gasifier. *Energy* **2007**, 32 (9), 1660–1669.
- (5) Zainal, Z. A.; et al. Prediction of performance of a downdraft gasifier using equilibrium modeling for different biomass materials. *Energy Convers. Manage.* **2001**, 42 (12), 1499–1515.
- (6) Sharma, A. K. Equilibrium modeling of global reduction reactions for a downdraft (biomass) gasifier. *Energy Convers. Manage.* **2008**, 49 (4), 832–842.
- (7) Melgar, A.; et al. Thermochemical equilibrium modelling of a gasifying process. *Energy Convers. Manage.* **2007**, 48 (1), 59–67.
- (8) Huang, H. J.; Ramaswamy, S. Modeling biomass gasification using thermodynamic equilibrium approach. *Appl. Biochem. Biotechnol.* **2009**, 154 (1–3), 193–204.
- (9) Wang, Y.; Kinoshita, C. M. Kinetic model of biomass gasification. *Sol. Energy* **1993**, 51 (1), 19–25.
- (10) Giltrap, D. L.; McKibbin, R.; Barnes, G. R. G. A steady state model of gas–char reactions in a downdraft biomass gasifier. *Sol. Energy* **2003**, 74 (1), 85–91.
- (11) Blasi, C. D. Dynamic behaviour of stratified downdraft gasifiers. *Chem. Eng. Sci.* **2000**, 55 (15), 2931–2944.
- (12) Shetha, P. N.; Babub, B. V. Modeling and simulation of downdraft biomass gasifier: Effect of char reactivity factor. *Energy Convers. Manage.* **2006**, 47 (15–16), 2602–2611.
- (13) Marklund, M.; Tegman, R.; Gebart, R. CFD modelling of black liquor gasification: Identification of important model parameters. *Fuel* **2007**, 86 (12–13), 1918–1926.
- (14) Fletcher, D. F.; et al. Computational fluid dynamics modelling of an entrained flow biomass gasifier. *Appl. Math. Modell.* **1998**, 22 (10), 747–757.

- (15) Xue, Q.; Heindel, T. J.; Fox, R. O. A CFD model for biomass fast pyrolysis in fluidized-bed reactors. *Chem. Eng. Sci.* **2011**, *66* (11), 2440–2452.
- (16) Papadikis, K.; Gu, S.; Bridgwater, A. V. CFD modelling of the fast pyrolysis of biomass in fluidised bed reactors. Part B: Heat, momentum and mass transport in bubbling fluidised beds. *Chem. Eng. Sci.* **2009**, *64* (5), 1036–1045.
- (17) Zhang, Q.; et al. Eulerian model for municipal solid waste gasification in a fixed-bed plasma gasification melting reactor. *Energy Fuels* **2011**, *25* (9), 4129–4137.
- (18) Gerun, L.; et al. Numerical investigation of the partial oxidation in a two-stage downdraft gasifier. *Fuel* **2008**, *87* (7), 1383–1393.
- (19) Donaj, P.; et al. Effect of pressure drop due to grate-bed resistance on the performance of a downdraft gasifier. *Energy Fuels* **2011**, *25* (11), 5366–5377.
- (20) Jones, W. P.; Launder, B. E. The prediction of laminarization with a two-equation model of turbulence. *Int. J. Heat Mass Transfer* **1972**, *15* (2), 301–314.
- (21) Cowin, S. C. A theory for the flow of granular materials. *Powder Technol.* **1974**, *9* (2–3), 61–69.
- (22) Schaeffer, D. G. Instability in the evolution equations describing incompressible granular flow. *J. Differ. Equations* **1987**, *66* (1), 19–50.
- (23) Syamlal, M.; Rogers, W. A.; O'Brien, T. J. *MFIX Documentation: Theory Guide*; National Technical Information Service: Springfield, VA, 1993; Technical Report DOE/METC-94/1004, NTIS/DE94000087.
- (24) Sarkar, S.; Lakshmanan, B. Applications of a Reynold-stress turbulence model to the compressible shear layer. *AIAA J.* **1991**, *29*, 743–749.
- (25) Kuipers, J. A. M.; et al. A numerical model of gas-fluidized beds. *Chem. Eng. Sci.* **1992**, *47* (8), 1913–1924.
- (26) Gunn, D. J. Transfer of heat or mass to particles in fixed and fluidised beds. *Int. J. Heat Mass Transfer* **1978**, *21* (4), 467–476.
- (27) Di Blasi, C.; et al. Product distribution from pyrolysis of wood and agricultural residues. *Ind. Eng. Chem. Res.* **1999**, *38* (6), 2216–2224.
- (28) Boroson, M. L.; et al. Product yields and kinetics from the vapor phase cracking of wood pyrolysis tars. *AIChE J.* **1989**, *35* (1), 120–128.
- (29) Di Blasi, C.; Branca, C. Kinetics of primary product formation from wood pyrolysis. *Ind. Eng. Chem. Res.* **2001**, *40* (23), 5547–5556.
- (30) Park, W. C.; Atreya, A.; Baum, H. R. Experimental and theoretical investigation of heat and mass transfer processes during wood pyrolysis. *Combust. Flame* **2010**, *157* (3), 481–494.
- (31) Hobbs, M. L.; Radulovic, P. T.; Smoot, L. D. Modeling fixed-bed coal gasifiers. *AIChE J.* **1992**, *38* (5), 681–702.
- (32) Donaj, P. Conversion of biomass and waste using highly preheated agents for materials and energy recovery. *Energy and Furnace Technology*; Royal Institute of Technology: Stockholm, Sweden, 2011.
- (33) Hobbs, M. L.; Radulovic, P. T.; Smoot, L. D. Combustion and gasification of coals in fixed-beds. *Prog. Energy Combust. Sci.* **1993**, *19* (6), 505–586.
- (34) Arthur, J. R. Reactions between carbon and oxygen. *Trans. Faraday Soc.* **1951**, *47*, 164–178.
- (35) Yoon, H.; Wei, J.; Denn, M. A model for moving-bed coal gasification reactors. *AIChE J.* **1978**, *24* (5), 885–903.
- (36) Siminski, V. L.; Wright, F. J.; Edelman, R. B.; Economos, C.; Fortune, O. F. *Research on Methods of Improving the Combustion Characters of Liquid Hydrocarbon Fuels. Volume I: Experimental Determination of Ignition Delay Times in Subsonic Flow Systems. Volume II: Kinetics Modeling and Supersonic Testing*; Air Force Aero Propulsion Laboratory, Air Force Systems Command: Wright-Patterson Air Force Base, OH, Feb 1972; AFAPL-TR-72-24.
- (37) Varma, A. K.; Chatwani, A. U.; Bracco, F. V. Studies of premixed laminar hydrogen air flames using elementary and global kinetics models. *Combust. Flame* **1986**, *64* (2), 233–236.
- (38) Howard, J. B.; Williams, G. C.; Fine, D. H. Kinetics of carbon monoxide oxidation in postflame gases. *Symp. (Int.) Combust., [Proc.]* **1973**, *14* (1), 975–986.
- (39) Macak, J.; Malecha, J. Mathematical model for the gasification of coal under pressure. *Ind. Eng. Chem. Process Des. Dev.* **1978**, *17* (1), 92–98.
- (40) Dryer, F. L.; Glassman, I. High-temperature oxidation of CO and CH<sub>4</sub>. *Symp. (Int.) Combust., [Proc.]* **1973**, *14* (1), 987–1003.
- (41) Jones, W. P.; Lindstedt, R. P. Global reaction schemes for hydrocarbon combustion. *Combust. Flame* **1988**, *73* (3), 233–249.